

Correlation between dislocation-density-based strain hardening and microstructural evolution in dual phase TC6 titanium alloy

Ran Shi^{a,b}, Zhihua Nie^a, Qunbo Fan^{a,b,*}, Fuchi Wang^{a,b}, Yu Zhou^{a,b}, Xin Liu^{a,b}

^a School of Materials Science and Engineering, Beijing Institute of Technology, Beijing 100081, China

^b National Key Laboratory of Science and Technology on Materials Under Shock and Impact, Beijing 100081, China



ARTICLE INFO

Keywords:

Titanium alloys
X-ray diffraction
Dislocation density
Strain hardening
Microstructures

ABSTRACT

Owing to their complex microstructures, the strain hardening of titanium alloys remains poorly understood. Therefore, the plastic deformation processes of the α and β phases in dual-phase TC6 (Ti–6Al–2.5Mo–1.5Cr–0.5Fe–0.3Si) titanium alloy were investigated via high-energy X-ray diffraction with in situ tensile loading. Dislocation density evolution in both the α and β phases was quantified via X-ray diffraction line profile analysis complemented by transmission electron microscopy measurements. The strain hardening rate calculated based on this evolution matched the strain hardening behaviors shown in the stress-strain curves. Furthermore, the effect of interactions between subgrain boundaries and slip systems were elucidated through transmission electron microscopy (TEM) observations. The evolution of strain hardening rate, as well as the dislocation density, was correlated with and well explained by the typical microstructures formed in different deformation regimes.

1. Introduction

Titanium alloys have been widely used in many industrial applications (ranging from biomedical applications to aerospace devices), owing to their attractive combination of mechanical properties [1–4]. The optimization of these improved mechanical properties in titanium-based alloys depends on the volume fraction, size, morphology, and distribution of the different phases that compose the microstructure. Shi et al. [5,6] have investigated the elastic-plastic deformation behavior of each constituent phase in $\alpha+\beta$ type dual-phase TC6 (Ti–6Al–2.5Mo–1.5Cr–0.5Fe–0.3Si) titanium alloy. However, the strain hardening behavior in the plastic deformation regime remains unexplored.

During deformation, the storage of dislocations in metals plays an important role in metallurgical phenomena, such as strain hardening, damage, creep, fatigue, recrystallization, athermal phase transformations, and strain-induced grain boundary migration [7]. The dislocation density, which is typically considered an internal-state-variable in models [8,9], has a significant effect on the plastic properties of alloys, especially the yield stress, hardness, strain hardening coefficient, and toughness [10]. The dislocation density is usually determined via direct-observation methods such as transmission electron microscopy (TEM) [11–13] and indirect methods, such as X-ray diffraction (XRD) [14–17]. The former method is rather complex and time consuming, owing to the demanding sample-preparation technique involved. The

latter method, which quantifies strain-induced changes in the dislocation density via XRD line profiles, has been significantly improved by using high-energy synchrotron XRD. In addition, the Williamson-Hall (W-H) plot analysis [18] provides a simplified integral breadth method, which considers the size-induced and strain-induced broadening of the peak width. These direct and indirect methods yield comparable dislocation density values.

The main objective of the present study is to quantify the dislocation density evolution of α and β phases in TC6 titanium alloy during tensile loading. The phase dislocation densities are determined via in-situ synchrotron-based XRD line profile analysis using the W-H method, complemented by TEM measurements. Furthermore, the strain hardening effect is investigated by calculating the hardening rate using Taylor law. The evolution of the strain hardening rate reflects an important deformation mechanism in materials subjected to tensile loading, as verified by TEM observations of the microstructural evolution.

2. Material and experimental procedures

A TC6 titanium alloy (Baoji Nonferrous Metal Works forged product, Baoji, China) was investigated in this work (see Table 1 for the chemical composition of the alloy). The as-received material was annealed at 800 °C for 2 h and then air-cooled. The room-temperature

* Corresponding author at: School of Materials Science and Engineering, Beijing Institute of Technology, Beijing 100081, China.
E-mail address: fanqunbo@bit.edu.cn (Q. Fan).

Table 1
Chemical composition of TC6 experimental alloy (wt%).

Element	Al	Mo	Cr	Fe	Si	C	N	H	Ti
wt%	6	2.5	1.5	0.5	0.3	< 0.07	< 0.03	< 0.01	Bal.

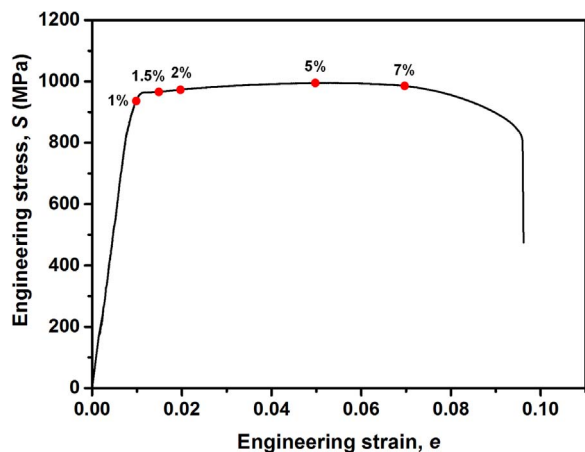


Fig. 1. Engineering stress-strain curve of TC6 titanium alloy loaded at a strain rate of $1 \times 10^{-4} \text{ s}^{-1}$.

macroscopic engineering stress (S)-strain (e) curve of the alloy loaded at a strain rate of $1 \times 10^{-4} \text{ s}^{-1}$ is shown in Fig. 1.

In-situ high-energy synchrotron XRD experiments were performed at the 11-ID-C beamline at the Advanced Photon Source, Argonne National Laboratory. A monochromatic X-ray beam (energy: 111 keV, wavelength: 0.11165 \AA) was used to map the lattice strain distributions of the specimen under uniaxial tensile loading. A detailed description of the preparation method and processing parameters has been provided in a previous paper [5]. The lattice strain distribution and evolution of different phases in the titanium alloy sheet were investigated by tracing the change in the lattice spacing with increasing load. The two-dimensional diffraction data were transformed to a one-dimensional line profile (intensity vs. 2°) by integrating over a $\pm 10^\circ$ azimuthal range around the axial/tensile direction of the specimen. The Bragg angle θ_{hkl} of the peak central position corresponding to each diffracting crystal plane was determined via Gaussian fitting. In this case, one or two Gaussian functions with different peak widths were fitted to an individual peak or overlapped peaks in the diffraction spectra. Furthermore, the evolution of the dislocation density as a function of the tensile strain was evaluated via peak broadening quantified by the full width at half maximum (FWHM) of the reflection.

Interrupted strain-controlled uniaxial tensile tests were then conducted with strain amplitudes (e) of 1%, 1.5%, 2%, 5%, and 7% (see Fig. 1). Dog-bone sheet specimens with an overall length of 34.29 mm and nominal gage dimensions of length: 10.16 mm, width: 3.175 mm, and thickness: 0.9 mm, were tested. Thin foil specimens (diameter: 3 mm) were first wire cut from the central part of the tensile specimens, mechanically thinned to $\sim 100 \mu\text{m}$, and then electropolished (at 30 V and -40°C) to perforation using a Tenupol twin-jet polishing unit. The electropolishing solution consisted of perchloric acid, methanol, and butanol at a volume ratio of 1:6:10. Images of the microstructure and the corresponding diffraction patterns were obtained on a Tencai G20 FEI (The Netherlands) microscope operated at 200 kV.

3. Results and discussion

3.1. Peak broadening analysis

The dislocation density can be indirectly determined from the XRD

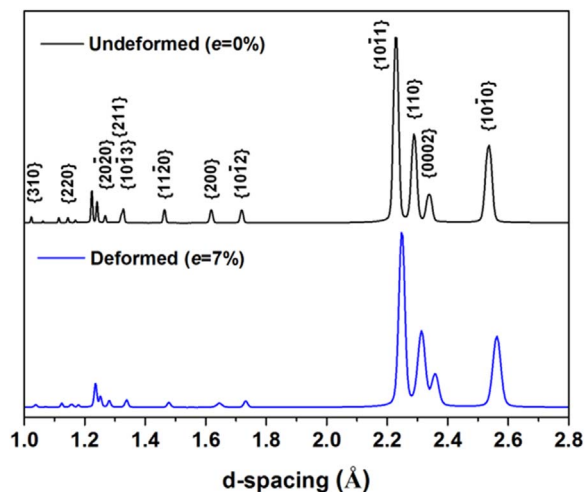


Fig. 2. One-dimensional line profiles (intensity vs. d-spacing) corresponding to the X-ray spectra of the undeformed ($e = 0\%$) and deformed ($e = 7\%$) samples. These profiles are obtained by integrating the Debye rings over a $\pm 10^\circ$ azimuthal range around the tensile direction.

profile [19]. The two-dimensional diffraction spectra are transformed to one-dimensional line profiles (intensity vs. d-spacing) by integrating the Debye rings over a $\pm 10^\circ$ azimuthal range around the tensile direction of the specimen (see Fig. 2). Evolution of the dislocation density of different phases is quantified via diffraction peak broadening (B) of the FWHM. In addition, using the W-H method, the crystal diameter (D) and microstrain (ϵ_{micro}) of the bulk samples are calculated from B . This method is a simplified integral breadth method where both size-induced and strain-induced broadening are deconvoluted by considering the peak width as a function of $2\theta_{hkl}$ [17]. Furthermore, this approach assumes that B consists of two broadening components namely, grain refinement broadening and strain broadening, which is given as:

$$B \cos \theta_{hkl} = \frac{\gamma \lambda}{D} + \epsilon_{micro} \sin \theta_{hkl} \quad (1)$$

where λ is the wavelength of radiation and $\gamma = 1$. After plotting $B \cos \theta_{hkl}$ vs. $\sin \theta_{hkl}$ and performing a linear regression analysis for each strain amplitude (Fig. 3), the values of D and ϵ_{micro} are obtained from the slope and intercept of the fitted lines.

The dislocation density (ρ) may be determined from [20,21]:

$$\rho = \frac{2\sqrt{3} \epsilon_{micro}}{Db} \quad (2)$$

Where, b is the Burgers vector. $\mathbf{b} = a/3 \langle 11-20 \rangle$ and $\mathbf{b} = a/2 \langle 111 \rangle$ -type dislocations in the α and β phases, respectively, are taken into account. The ρ values obtained from Eq. (2) are plotted as a function of the true strain (ϵ) (see Fig. 4). During plastic deformation of a material, the dislocation density increases leading to strain hardening of the material. Owing to pre-processing and, hence, pre-existing dislocations, the α and β phases both have non-zero ρ values (in this case, $1.17 \times 10^{14} \text{ m}^{-2}$ and $2.45 \times 10^{14} \text{ m}^{-2}$, respectively). The dislocation density of the α phase (ρ_α) increases significantly from $1.88 \times 10^{14} \text{ m}^{-2}$ at point A ($\epsilon = 0.73\%$) to $3.36 \times 10^{14} \text{ m}^{-2}$ at point B ($\epsilon = 1.02\%$) and then plateaus until point C ($\epsilon = 1.30\%$). The β phase starts to plastically deform later than the α phase. Therefore, the dislocation density of the β phase (ρ_β) increases slightly (from $3.36 \times 10^{14} \text{ m}^{-2}$ to $3.79 \times 10^{14} \text{ m}^{-2}$) at first and then increases sharply (to $4.87 \times 10^{14} \text{ m}^{-2}$). The interactions of the stress and strain behavior of the α and β phases during this elastic-plastic transition process were reported in our previous paper [5]. Therefore, in the present study, we focus on the evolution in the plastic regime. When both phases begin to deform plastically, ρ_α increases continuously, whereas ρ_β starts to fluctuate at $\epsilon = 4\%$, and decreases thereafter. This results from the fact that the body-centered cubic (BCC)

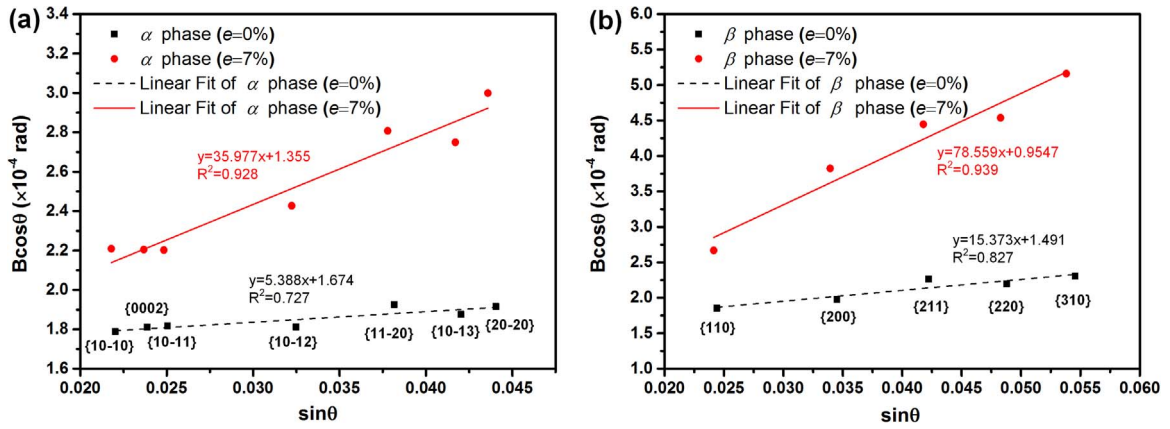


Fig. 3. $B\cos\theta_{hkl}$ vs. $\sin\theta_{hkl}$ for the (a) α phase and (b) β phase. Dashed line: linear regression fit for $e = 0\%$; Solid line: linear regression fit for $e = 7\%$.

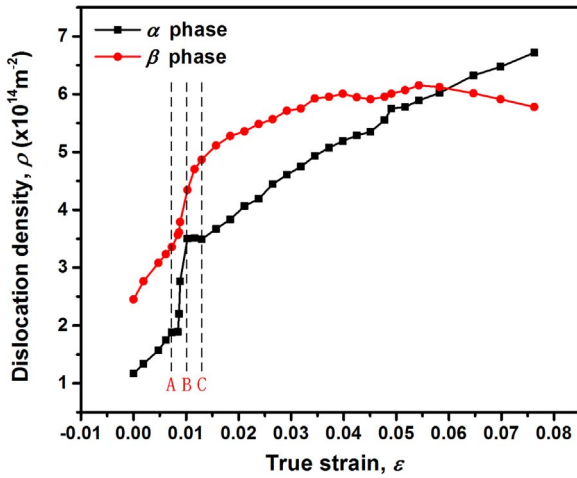


Fig. 4. Dislocation density of the α and β phases as a function of the applied true strain.

β phase has more slip systems and a higher stacking-fault energy than the hexagonal close-packed (HCP) α phase. Therefore, dislocation climb and cross-slip occur more easily and, hence, dislocation accumulation and the corresponding increase in the dislocation density are more difficult in the β phase than in the α phase [22].

The Taylor equation is used to describe work hardening, which directly relates the flow stress and the dislocation density of a material [23,24]. The flow stress τ of a material may be expressed as follows:

$$\tau = \tau_0 + \eta Gb\sqrt{\rho} \quad (3)$$

where, τ_0 : flow stress of the material in the absence of dislocation interactions (strain hardening), η (usually denoted as α in the literature, here η is used to avoid confusion with the α phase): dimensionless parameter ranging from 0.05 to 2.6 for different materials [25], G : shear modulus, and b : Burgers vector. The Taylor factor, M , which relates the shear flow stress τ of a single crystal to the uniaxial flow stress σ of a polycrystalline, is usually taken as 3.0 [26–28]. The Taylor equation can be reformulated for the uniaxial loading of a polycrystalline,

$$\sigma = \sigma_0 + M\eta Gb(\sqrt{\rho} - \sqrt{\rho_0}) \quad (4)$$

where, σ_0 : yield stress and ρ_0 : corresponding dislocation density. Using Taylor law, the strain-hardening rate, θ_p , of a polycrystalline metal may be expressed as:

$$\theta_p \equiv \frac{d\sigma}{d\varepsilon_p} = \frac{\eta G M b}{2\sqrt{\rho}} \frac{d\rho}{d\varepsilon_p} \quad (5)$$

where, ε_p is the plastic strain, $\varepsilon_p = \varepsilon - \sigma/E$.

The experiment was performed in strain-control mode and, therefore we assumed that the strain of the α phase (ε_α) and the β phase (ε_β) is equal to the applied true strain (ε). However, due to the difference in the Young's moduli of the phases, the stress states in these phases differ from the applied stress. We determine the stress state in each phase by substituting the measured ρ and the initial yield stresses (σ_0^α : 877.8 MPa; σ_0^β : 969 MPa) into Taylor law (α phase: $\eta = 0.31$; β phase: $\eta = 0.33$) [6]. The average (overall) stress (σ) depends on the stress in each phase and the volume fraction of the given phase, i.e., $\sigma = f^\alpha \sigma^\alpha + f^\beta \sigma^\beta$ (the phase volume fractions of the α and the β phases (f^α , f^β) are 81.8% and 18.2%, respectively). Therefore, the stress of the α and β phases can be separated by using the dislocation-dependent Taylor law. As Fig. 5(a) shows, the experimentally determined phase volume fraction mixed true stress-strain curves and their calculated counterparts exhibit similar trends.

Fig. 5(a) also shows the macroscopic strain hardening rate ($d\sigma/d\varepsilon$) obtained from the experimental true stress-strain curve. In our previous work [6], initial yield stresses of 110.3 GPa and 104.5 GPa were determined for the α and β phases, respectively, by using the elastic-plastic self-consistent (EPSC) framework. The ε_p of each phase considered in the present study is calculated and the derivative of the corresponding strain hardening rates θ_p is then plotted (see Fig. 5(b)). Initially, the macroscopic strain hardening rate decreases sharply with increasing strain. This decrease is followed by a declination with fluctuation after the sample enters the stage of fully plastic flow. The trend changes abruptly at $\sim 5\%$ strain. In fact, the macroscopic strain hardening decreases at strain values higher than 6.5%. A similar trend is observed for the phase strain hardening rate θ_p . The trend observed for the θ_p of the α phase, during the initial stage ($\varepsilon \leq 1.30\%$), differs from that observed for the θ_p of the β phase. The sharp decrease in θ_p of the α phase and the subsequent rapid increase, is attributed to the transition from the elastic to the elasto-plastic regime. The θ_p of both phases change abruptly at ε values of $5.03 \pm 0.79\%$. A similar increase in the macroscopic strain hardening rate has been observed in Ti-9Mo-6W, Ti-12Mo, and Ti-8.5Cr-1.5Sn [29,30] titanium alloys and twinning induced plasticity steels (Fe-20Mn-0.6C) [31] subjected to tensile testing. The same trend was also observed for AZ31B magnesium alloy [32] and commercially pure titanium [33] subjected to compression tests. This increase has been attributed to deformation twinning. However, the Mo content of the TC6 titanium alloy (2.5 wt%) is lower than that required to induce deformation twinning. This indicates that deformation in the present samples proceeds via some other mechanism. To identify this mechanism, we investigate the microstructural evolution of the material. In the final stage of deformation, the θ_p of both phases converges to a constant, which is positive for the α phase and negative for the β phase. This suggests that the drop in the macroscopic strain hardening rate curve results mainly from the softening of the β phase.

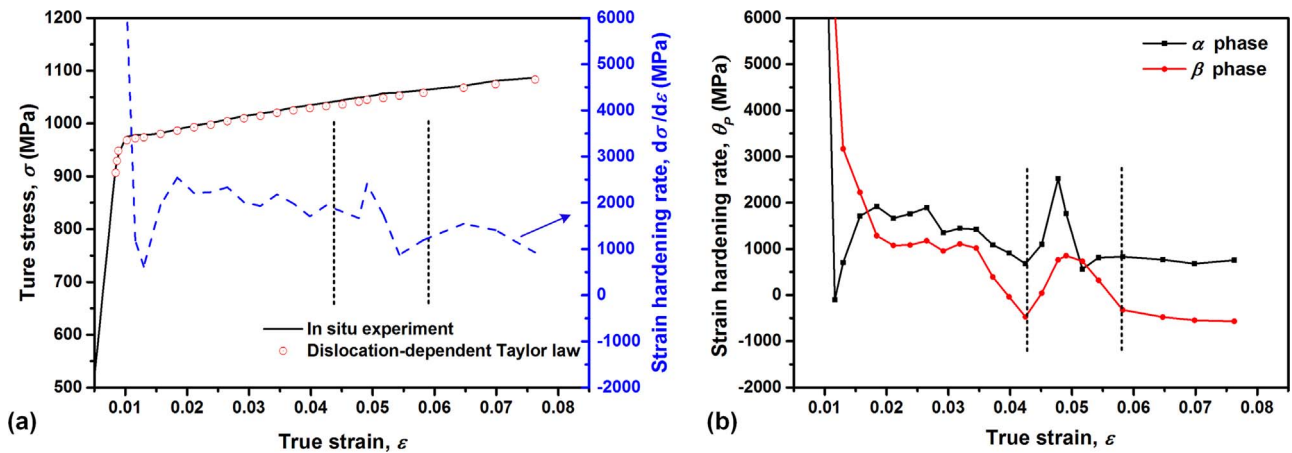


Fig. 5. (a) Calculated phase volume fraction mixed stress (dots), experimentally measured stress (solid line), and strain hardening rate ($d\sigma/d\varepsilon$), obtained from the experimental true stress-strain curve (dashed line), as a function of the applied true strain. (b) Strain hardening rate (θ_p) of the α and β phases as a function of the applied true strain.

3.2. TEM analysis

The microstructural evolution in five samples subjected to strain amplitudes (ε) of 1%, 1.5%, 2%, 5%, and 7% (see Fig. 1) is investigated via TEM. Fig. 6 shows the dislocation microstructure at 1% strain, which lies within the elastic-plastic transition stage. The elastic deformation is recovered after unloading. Furthermore, only a few plastic-deformation features are retained in the nano-level dislocation configurations (Fig. 6(a)) at grain boundaries and simple dislocation lines (Fig. 6(b)).

Fig. 7 shows the dislocation microstructure at 1.5% strain. In this stage, irreversible plastic deformation is stored in the form of dislocation tangles (indicated by the arrows in Fig. 7(a)). Moreover, the strain-induced α -to- β phase transformation, described by the $\{11\bar{2}0\}_\alpha // \{200\}_\beta$ orientation relation (see Fig. 7(b)), occurs at this strain level. Plane A in the figure corresponds to $\{11\bar{2}0\}_\alpha$. From the reciprocal diffraction spot, values of 2.083 Å and 1.466 Å are calculated for the $\{110\}_\beta$ and $\{002\}_\beta$ planes, respectively. These values are both lower than the corresponding standard values (2.348 Å and 1.660 Å), indicating that the β phase is in the compressive state.

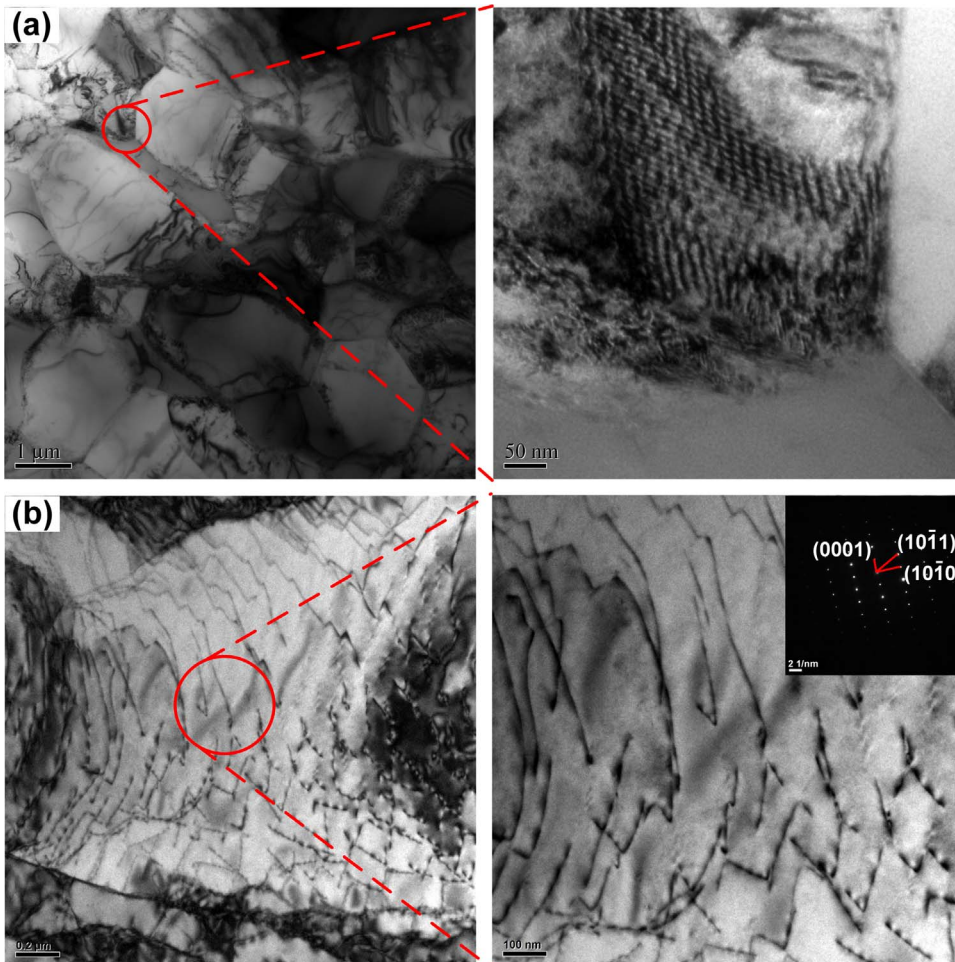


Fig. 6. TEM bright-field micrographs of the sample subjected to 1% strain, (a) nano-level dislocation configurations, (b) dislocation lines.

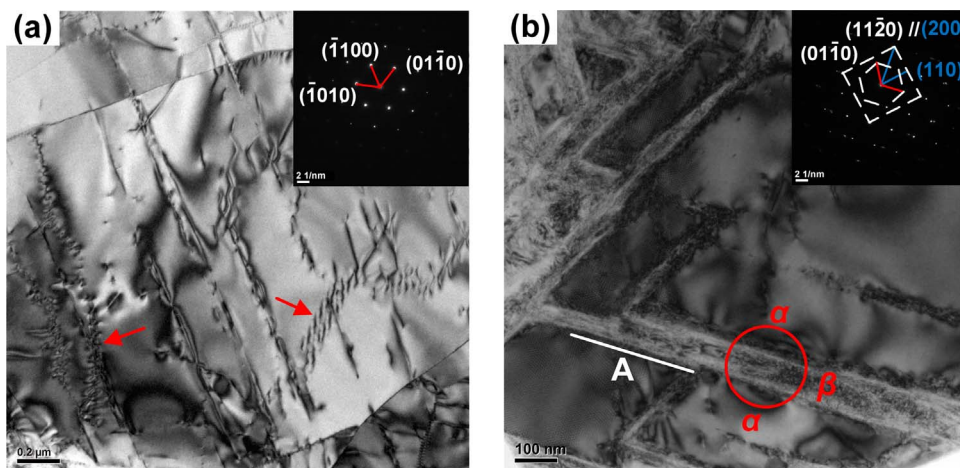


Fig. 7. TEM bright-field micrographs of the sample subjected to 1.5% strain, (a) dislocation tangles, (b) strain-induced phase transformation from the α phase to the β phase.

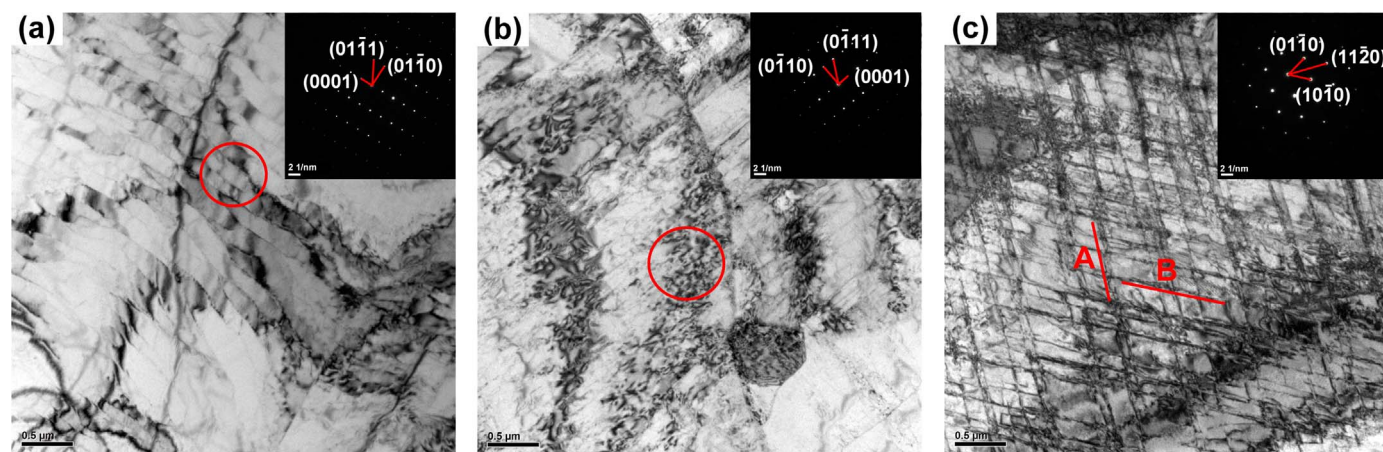


Fig. 8. TEM bright-field micrographs of samples subjected to: (a) 2% strain, showing numerous subgrain boundaries formed by dislocations, (b) 5% strain, showing curved and tangled dislocation lines, (c) 7% strain, showing a criss-crossing dislocation pattern.

With loading, interactions between dislocations increase leading to a mass of dislocation arrays and cells. The cell wall has high dislocation density, and the cell interior is a low-density dislocation region. An image of a typical dislocation microstructure at 2% strain is shown in Fig. 8(a). As the figure shows, the dislocations of slip systems associated with a particular direction in the α phase form numerous subgrain boundaries. At 5% strain, slip systems associated with another direction are activated, and the subgrain boundaries (formed by dislocations of the first direction) act as obstacles, as shown in nanopillar compression tests [34]. The interaction between slip systems associated with different directions leads to curved dislocation lines and dislocation tangles (see Fig. 8(b)) and, in turn, strain hardening (see Fig. 5). When the strain increases to 7%, the dislocation tangles are broken and shear banding begins (as indicated by the engineering strain-stress curve in Fig. 1, after 7% strain, significant softening occurs and the stress decreases). Dislocations on planes A $\{11\bar{2}0\}_{\alpha}$ and B $\{\bar{1}2\bar{1}0\}_{\alpha}$ form a criss-crossing dislocation pattern, as shown in Fig. 8(c).

4. Discussion

The results of our in situ X-ray measurements are correlated with TEM observations of dislocations within subgrains. Here, we focus only on dislocation measurements in the major phase α , owing to its high volume fraction. The intragranular dislocation density is determined by manually measuring the projected length of the dislocation lines (l_p) in the TEM images, using the open-source image analysis program Image J [35]. These measurements consisted of the following image processing steps (see Fig. 9 for a schematic of the process).

- (1) Process – Enhance Contrast: to enhance the contrast between dark dislocation lines and the light background;
- (2) Process – Math – Multiply: with value of 1.5 to further enhance the contrast;
- (3) Process – Binary – Make Binary: to convert the image into a binary image;
- (4) Analyze – Skeleton – Analyze Skeleton (2D/3D): to repeatedly reduce the objects in a binary image to single-pixel-wide shapes and measure their length.

The sum of the length of the dislocation lines is l_p . By assuming that the (i) testing region of a TEM foil thickness (t) is ~ 100 nm and (ii) dislocations are randomly oriented, l_p can be correlated with the length of the dislocation lines. The dislocation density of the region of interest, A , is then determined from:

$$\rho = \frac{l_p}{V} = \frac{l_p}{At} \quad (6)$$

The TEM-determined average ρ values of the α phase are lower than the XRD-determined values, especially at low strain levels (Fig. 10). Factors such as the systematic error within the random line method, the invisibility of certain dislocations, and inaccurate measurement of the foil thickness may influence the values determined from TEM measurements. Additionally, TEM measurements only represent a small sample area, while XRD measurements reveal details of the bulk deformed material. Other uncertainties associated with TEM measurements and XRD line profile analysis have been discussed extensively in the literature [36–39]. However, as the dislocation density increases,

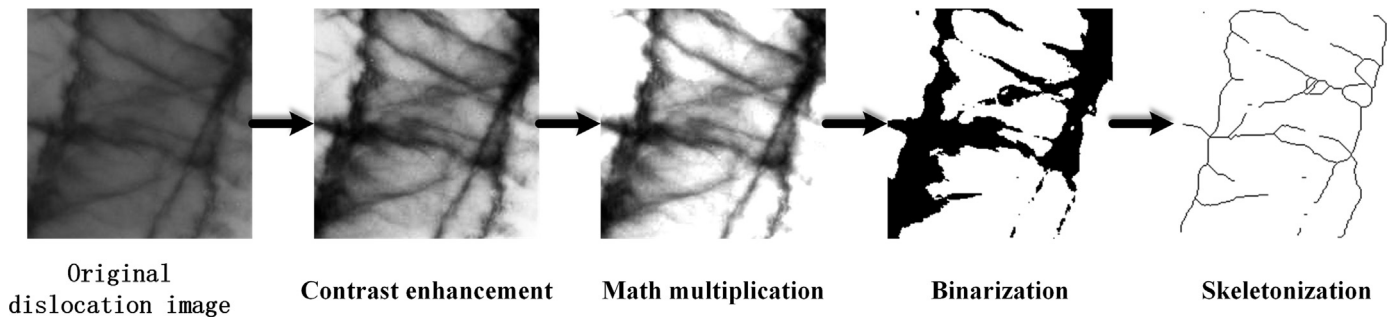


Fig. 9. Image processing steps for extraction of the projected length of dislocation lines in TEM images.

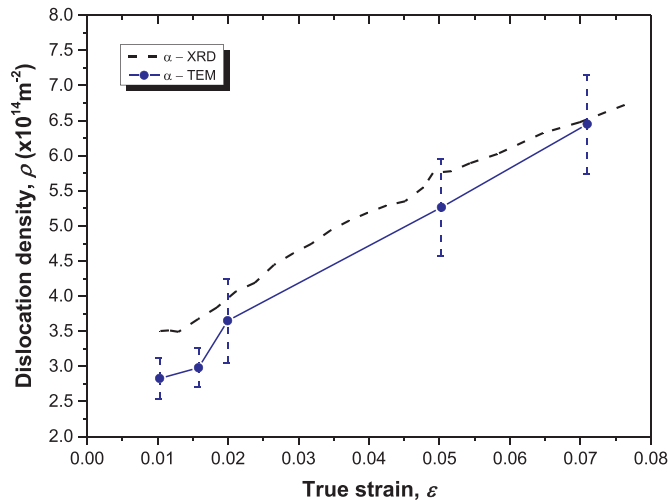


Fig. 10. Dislocation density ρ , measured via the indirect XRD method and direct TEM observations, as a function of the applied true strain.

the TEM-measured ρ (average \pm standard deviation) approaches the XRD-determined value and the values converge eventually. Therefore, in the case of clearly distinguishable dislocations, these measurements yield comparable results. According to Gutierrez-Urrutia and Raabe [7], TEM measurements yield highly accurate results for dislocation densities ranging from $5 \times 10^{14} \text{m}^{-2}$ to $10 \times 10^{14} \text{m}^{-2}$.

5. Conclusions

The dislocation density and strain hardening rate of the α and β phases in a dual-phase TC6 titanium alloy were investigated via high-energy XRD, with in situ tensile loading, complemented by TEM observations. The conclusions of this study are summarized as follows:

- After the material enters the stage of fully plastic flow, the dislocation density of the α phase increases continuously. However, the dislocation density of the β phase increases until the strain reaches 4% and decreases thereafter.
- The dislocation-density-based strain hardening rate of the α and β phases changed abruptly at a strain of $\sim 5\%$. In addition, TEM observations revealed that the subgrain boundaries act as obstacles when slip systems associated with differing directions intersect. The interaction between these slip systems resulted in curved dislocation lines and tangled dislocation lines, leading to an increase in the strain hardening rate.
- In the ending stage of deformation, the drop in the macroscopic strain hardening rate curve resulted mainly from the softening of the β phase, as evidenced by the phase strain hardening rate converging to a negative constant.
- The agreement between the XRD- and TEM-measured dislocation

density values of the α phase improved with increasing value of this density.

Therefore, the relationship between dislocation-density-based strain hardening and microstructural evolution has been elucidated.

Acknowledgements

We gratefully acknowledge the funding support from project 51571031 of the Chinese National Natural Science Foundation. Use of the Advanced Photon Source was supported by the US Department of Energy, Office of Science Laboratory, Office of Basic Energy Sciences, under contract DE-AC02-06CH11357.

References

- [1] F. Guillemot, F. Prima, R. Bareille, D. Gordin, T. Gloriant, M.C. Porte-Durrieu, D. Ansel, C.H. Baquey, Design of new titanium alloys for orthopaedic applications, *Med. Biol. Eng. Comput.* 42 (2004) 137–141.
- [2] M. Niinomi, Mechanical biocompatibilities of titanium alloys for biomedical applications, *J. Mech. Behav. Biomed. Mater.* 1 (2008) 30–42, <http://dx.doi.org/10.1016/j.jmbbm.2007.07.001>.
- [3] C.H. Pei, Q.B. Fan, H.N. Cai, J.C. Li, High temperature deformation behavior of the TC6 titanium alloy under the uniform DC electric field, *J. Alloy. Compd.* 489 (2010) 401–407.
- [4] F. Sun, F. Prima, T. Gloriant, High-strength nanostructured Ti–12Mo alloy from ductile metastable beta state precursor, *Mater. Sci. Eng. A* 527 (2010) 4262–4269, <http://dx.doi.org/10.1016/j.msea.2010.03.044>.
- [5] R. Shi, Z. Nie, Q. Fan, G. Li, Elastic plastic deformation of TC6 titanium alloy analyzed by in-situ synchrotron based X-ray diffraction and microstructure based finite element modeling, *J. Alloy. Compd.* 688 (2016) 787–795, <http://dx.doi.org/10.1016/j.jallcom.2016.07.105>.
- [6] R. Shi, G. Li, Z. Nie, Q. Fan, Determination of the single-phase constitutive relations of α/β dual phase TC6 titanium alloy, *Mater. Sci. Eng. A* 675 (2016) 138–146, <http://dx.doi.org/10.1016/j.msea.2016.08.057>.
- [7] I. Gutierrez-Urrutia, D. Raabe, Dislocation density measurement by electron channeling contrast imaging in a scanning electron microscope, *Scr. Mater.* 66 (2012) 343–346, <http://dx.doi.org/10.1016/j.scriptamat.2011.11.027>.
- [8] J. Luo, M. Li, X. Li, Y. Shi, Constitutive model for high temperature deformation of titanium alloys using internal state variables, *Mech. Mater.* 42 (2010) 157–165, <http://dx.doi.org/10.1016/j.mechmat.2009.10.004>.
- [9] Z.C. Sun, H. Yang, G.J. Han, X.G. Fan, A numerical model based on internal-state-variable method for the microstructure evolution during hot-working process of TA15 titanium alloy, *Mater. Sci. Eng. A* 527 (2010) 3464–3471, <http://dx.doi.org/10.1016/j.msea.2010.02.009>.
- [10] S. Graça, R. Colaço, P.A. Carvalho, R. Vilar, Determination of dislocation density from hardness measurements in metals, *Mater. Lett.* 62 (2008) 3812–3814, <http://dx.doi.org/10.1016/j.matlet.2008.04.072>.
- [11] T. Mayer, L. Balogh, C. Solenthaler, E. Mu, S.R. Holdsworth, Dislocation density and sub-grain size evolution of 2CrMoNiWV during low cycle fatigue at elevated temperatures, *Acta Mater.* 60 (2012) 2485–2496, <http://dx.doi.org/10.1016/j.actamat.2011.12.031>.
- [12] S. Zherebtsov, E. Kudryavtsev, S. Kostjuchenko, S. Malysheva, G. Salishchev, Strength and ductility-related properties of ultrafine grained two-phase titanium alloy produced by warm multiaxial forging, *Mater. Sci. Eng. A* 536 (2012) 190–196, <http://dx.doi.org/10.1016/j.msea.2011.12.102>.
- [13] M. Li, L. Wang, J.D. Almer, Dislocation evolution during tensile deformation in ferritic – martensitic steels revealed by high-energy X-rays, *Acta Mater.* 76 (2014) 381–393, <http://dx.doi.org/10.1016/j.actamat.2014.05.026>.
- [14] T. Shintani, Y. Murata, Evaluation of the dislocation density and dislocation character in cold rolled Type 304 steel determined by profile analysis of X-ray diffraction, *Acta Mater.* 59 (2011) 4314–4322, <http://dx.doi.org/10.1016/j.actamat.2011.03.055>.

- [15] T. Ungár, J. Gubicza, P. Hanák, I. Alexandrov, Densities and character of dislocations and size-distribution of subgrains in deformed metals by X-ray diffraction profile analysis, *Mater. Sci. Eng. A* 321 (2001) 274–278.
- [16] Z.Y. Zhong, H. Brokmeier, W.M. Gan, E. Maawad, B. Schwebke, N. Schell, Materials characterization dislocation density evolution of AA 7020-T6 investigated by in-situ synchrotron diffraction under tensile load, *Mater. Charact.* 108 (2015) 124–131, <http://dx.doi.org/10.1016/j.matchar.2015.09.004>.
- [17] S.E. Shin, D.H. Bae, Deformation behavior of aluminum alloy matrix composites reinforced with few-layer graphene, *Composites Part A* 78 (2015) 42–47, <http://dx.doi.org/10.1016/j.compositesa.2015.08.001>.
- [18] C. Suryanarayana, M.G. Norton, *X-ray Diffraction: A Practical Approach*, Springer Science & Business Media, 2013.
- [19] L. Lutterotti, S. Gialanella, X-ray diffraction characterization of heavily deformed metallic specimens, *Acta Mater.* 46 (1998) 101–110.
- [20] G.K. Williamson, W.H. Hall, The use of Fourier analysis in the interpretation of X-ray line broadening from cold-worked iron and molybdenum, *Acta Crystallogr.* 1 (1954) 574–581.
- [21] R.E. Smallman, K.H. Westmacott, Stacking faults in face-centred cubic metals and alloys, *Philos. Mag.* 2 (1957) 669–683.
- [22] Z.C. Sun, H. Yang, G.J. Han, X.G. Fan, A numerical model based on internal-state-variable method for the microstructure evolution during hot-working process of TA15 titanium alloy, *Mater. Sci. Eng. A* 527 (2010) 3464–3471.
- [23] G.I. Taylor, The mechanism of plastic deformation of crystals. Part I- theoretical, *Proc. R. Soc. London. Ser. A Contain. Pap. Math. Phys. Charact.* 145 (1934) 362–387.
- [24] C. Tomchik, J. Almer, O. Anderoglu, L. Balogh, D.W. Brown, B. Clausen, S.A. Maloy, T.A. Sisneros, J.F. Stubbins, High energy X-ray diffraction study of the relationship between the macroscopic mechanical properties and microstructure of irradiated HT-9 steel, *J. Nucl. Mater.* 475 (2016) 46–56, <http://dx.doi.org/10.1016/j.jnucmat.2016.03.023>.
- [25] F. Lavrentev, The type of dislocation interaction as the factor determining work hardening, *Mater. Sci. Eng.* 46 (1980) 191–208.
- [26] G.I. Taylor, Plastic strain in metals, *J. Inst. Met.* 62 (1938) 307–324.
- [27] U.F. Kocks, The relation between polycrystal deformation and single-crystal deformation, *Metall. Mater. Trans.* 1 (1970) 1121–1143.
- [28] R.E. Stoller, S.J. Zinkle, On the relationship between uniaxial yield strength and resolved shear stress in polycrystalline materials, *J. Nucl. Mater.* 287 (2008) 349–352.
- [29] F. Sun, J.Y. Zhang, M. Marteleur, C. Brozek, E.F. Rauch, M. Veron, A new titanium alloy with a combination of high strength, high strain hardening and improved ductility, *Scr. Mater.* 94 (2015) 17–20, <http://dx.doi.org/10.1016/j.scriptamat.2014.09.005>.
- [30] C. Brozek, F. Sun, P. Vermaut, Y. Millet, A. Lenain, D. Embury, P.J. Jacques, F. Prima, A β -titanium alloy with extra high strain-hardening rate: Design and mechanical properties, *Scr. Mater.* 114 (2016) 60–64, <http://dx.doi.org/10.1016/j.scriptamat.2015.11.020>.
- [31] Y.F. Shen, N. Jia, R.D.K. Misra, L. Zuo, Softening behavior by excessive twinning and adiabatic heating at high strain rate in a Fe–20Mn–0.6C TWIP steel, *Acta Mater.* 103 (2016) 229–242, <http://dx.doi.org/10.1016/j.actamat.2015.09.061>.
- [32] S.C. Li, Z.S. Zhang, H.S. Ming, Deformation mechanism of AZ31B magnesium alloy under different loading paths, *Acta Metall. Sin. (Engl. Lett.)* 28 (2015) 1426–1434, <http://dx.doi.org/10.1007/s40195-015-0342-5>.
- [33] K. Ahn, H. Huh, J. Yoon, Rate-dependent hardening model for pure titanium considering the effect of deformation twinning, *Int. J. Mech. Sci.* 98 (2015) 80–92, <http://dx.doi.org/10.1016/j.ijmecsci.2015.04.008>.
- [34] S. Papanikolaou, H. Song, E. Van Der Giessen, Obstacles and sources in dislocation dynamics: strengthening and statistics of abrupt plastic events in nanopillar compression, *J. Mech. Phys. Solids* 102 (2017) 17–29, <http://dx.doi.org/10.1016/j.jmps.2017.02.004>.
- [35] T. Ferreira, W. Rasband, *The ImageJ User Guide – Version 1.46r*. <<https://imagej.nih.gov/ij/docs/guide/user-guide.pdf>> (October, 2012).
- [36] R.K. Ham, N.G. Sharpe, A systematic error in the determination of dislocation densities in thin films, *Philos. Mag.* 69 (1961) 1193–1194, <http://dx.doi.org/10.1080/14786436108239683>.
- [37] R.K. Ham, The determination of dislocation densities in thin films, *Philos. Mag.* 69 (1961) 1183–1184, <http://dx.doi.org/10.1080/14786436108239679>.
- [38] L. Balogh, L. Capolungo, C.N. Tome, On the measure of dislocation densities from diffraction line profiles: a comparison with discrete dislocation methods, *Acta Mater.* 60 (2012) 1467–1477, <http://dx.doi.org/10.1016/j.actamat.2011.10.037>.
- [39] T. Ungar, G. Tichy, The effect of dislocation contrast on X-ray line profiles in untextured polycrystals, *Phys. Status Solidi* 171 (1999) 425–434.